Acta Materialia 95 (2015) 274–283

Contents lists available at ScienceDirect

Acta Materialia

journal homepage: www.elsevier.com/locate/actamat

Effect of ruthenium on the precipitation of topologically close packed phases in Ni-based superalloys of 3rd and 4th generation

K. Matuszewski [a,*], R. Rettig [a], H. Matysiak [d], Z. Peng [b], I. Povstugar [b], P. Choi [b], J. Müller [c], D. Raabe [b], E. Spiecker [c], K.J. Kurzydłowski [d], R.F. Singer [a]

[a] University of Erlangen-Nuremberg FAU, Department of Materials Science and Engineering, Institute of Science and Technology of Metals WTM, Martensstr. 5, 91058 Erlangen, Germany
[b] Max-Planck-Institut für Eisenforschung GmbH, Department of Microstructure Physics and Alloy Design, Max-Planck-Str. 1, 40237 Düsseldorf, Germany
[c] University of Erlangen-Nuremberg FAU, Department of Materials Science and Engineering, Center for Nanoanalysis and Electron Microscopy, Cauerstr. 6, 91058 Erlangen, Germany
[d] Warsaw University of Technology, Faculty of Materials Science and Engineering, Materials Design Division, Woloska 141, 02-507 Warsaw, Poland

ARTICLE INFO

Article history:
Received 23 January 2015
Revised 13 April 2015
Accepted 3 May 2015

Keywords:
Topologically close packed (TCP) phases
Ni-based superalloys
Precipitation
Ruthenium effect
Thermodynamics

ABSTRACT

The precipitation of topologically close packed (TCP) phases is detrimental for the high temperature strength of high refractory Ni-based superalloys. The beneficial influence of Ru with respect to this so called instability is nowadays well accepted. In the present paper the precipitation of topologically close packed (TCP) phases is studied quantitatively in two experimental alloys (one Ru-free and one with addition of Ru) to clarify the mechanism of the Ru effect. It is confirmed that the TCP phase precipitates undergo sequential phase transformation with the tetragonal σ-phase precipitating first. Ru retards the phase transformation and leads to decreased equilibrium volume fraction of TCP phases. The results clearly indicate that Ru decreases the driving force for TCP phase precipitation. Investigations of crystallography and chemistry of the TCP/matrix interface point to an additional effect by increase of misfit strain energy.

1. Introduction

High-temperature strength of nickel based superalloys is strongly dependent on the content of refractory elements, particularly Re. The beneficial characteristic of Re is attributed to its high solid solution strengthening effect [1–3], high melting point and a very low diffusion coefficient [4,5]. Quantitatively, the effect of Re depends on the alloy composition. As reported by Heckl, addition of 1 at.% Re can improve the high-temperature capability by up to 87 K [6]. However, beside the beneficial effect, the very low diffusion coefficient of Re also brings about some disadvantages. Considering the as cast microstructure, strong segregation of Re to the dendrite core demands the application of expensive homogenization heat-treatments [7,8]. Moreover, Re induces precipitation of topologically close packed (TCP) phases during long-term high-temperature exposition [9–14]. TCP phases are very detrimental because of two main factors. At first, when they nucleate and grow, they deplete the γ-matrix phase from solid solution strengtheners. This leads to decreased creep resistance of the material [10,14]. Further, TCP phases are brittle and exhibit a complex lath- or plate-like morphology [15], which evolves with time [16]. Thus, cracks are easily nucleated. As a consequence the fatigue life-time and tensile ductility of the material will be decreased [14].

It is widely accepted that precipitation of TCP phases can be suppressed by an addition of ruthenium. Several possible mechanisms for this effect were proposed based on experiments [10,17–20] and simulations [21,22]. Among the solubility related mechanisms, 'reverse partitioning' [18–20] or increased solubility of Re and W within the γ-matrix phase [10,17] was suggested. Alternatively, a change in TCP/matrix interface energy [21,22] was considered as a potent factor influenced by Ru. However, as TCP phases exhibit very small sizes in the early stages of precipitation and are very sensitive to alloy chemistry, it was difficult to draw the final conclusions without advanced high-resolution characterization and quantitative description of phase transformation.

Recently the present authors [16] used the Johnson–Mehl–Avrami equation to describe the precipitation of TCP phases [23]. It was found that ruthenium influences both nucleation and growth rate of TCP phases. This observation indicates that Ru affects the interface energy or the chemical driving force for TCP phase

* Corresponding author. Tel.: +49 9131 85 20334; fax: +49 9131 85 27515.
E-mail address: kamil.matuszewski@ww.uni-erlangen.de (K. Matuszewski).

http://dx.doi.org/10.1016/j.actamat.2015.05.033
1359-6454/

formation. The TCP phases undergo a precipitation sequence [9,11,16] and thus it is most relevant to understand the Ru influence on the nucleation of the first TCP particles. Nevertheless, the mechanism of TCP phase growth also needs to be studied.

In the present paper we describe the precipitation process of TCP phases by combining crystallographic and compositional data obtained by transmission electron microscopy (TEM) and atom probe tomography (APT), respectively. We complement these results with the standard two-dimensional (2D) and advanced three-dimensional (3D) microscopic observations. Based on the results, conclusions on the influence of Ru on the precipitation of TCP phases are drawn.

2. Experimental

2.1. Material

Astra 1–20 and Astra 1–21, two experimental nickel based superalloys of the 3rd and 4th generation, respectively, were used to investigate the influence of Ru on the early stages of TCP phase precipitation. The detailed chemical compositions of the two alloys are given in Table 1. The designation Astra refers to a series of experimental alloys developed in our laboratory based vaguely on the commercial alloy CMSX-4 [6,7]. Both alloys studied here, Astra 1–20 and Astra 1–21, contain 2 at.% of Re. The two alloys differ only in Ru content. While Astra 1–20 has no additional Ru, Astra 1–21 contains 1 at.% Ru. Ru is being added at the expense of Ni. The definition of the alloys in at.% allows to keep the content of all other alloying elements constant, i.e. avoids unintended additional compositional changes.

Materials were produced in a vacuum arc furnace. Subsequently directional solidification in a lab-scale Bridgman vacuum induction melting furnace was used to convert them into columnar grained structures. A cluster of three cylindrical rods with a diameter of 12 mm and a height of 180 mm was cast with a withdrawal rate of 9 mm min^{-1}. This resulted in a primary dendrite arm (PDA) spacing of 180 μm. All details of the casting process can be found in [7].

A three step heat-treatment was applied after the casting process. In the first step the alloys were homogenized at 1340 °C for 16 h to reduce the segregation of refractory elements. Two subsequent aging steps were conducted to precipitate γ′ particles and stabilize their morphology. The detailed parameters of the heat-treatment procedure are given in Table 2. Experimental evidence suggested that the same heat-treatment conditions can be used for both alloys with and without addition of Ru [7].

Specimens of 10 mm in height and 12 mm in diameter were cut from heat-treated samples. The small specimens were then annealed at various time–temperature conditions. The present paper focuses on the materials annealed at 950 °C between 500 and 2000 h with 500 h intervals. All the steps of standard heat-treatment as well as high-temperature exposition were conducted in Ar atmosphere.

The annealed samples were prepared for microscopic observations via standard metallographic operations, i.e. gradual grinding and polishing.

Table 1
Chemical compositions of investigated alloys (at.% and wt.%). The designation Astra refers to a series of in-house experimental alloys approximately based on commercial second generation superalloy CMSX-4. The two alloys investigated here, Astra 1–20 and 1–21, differ only in Ru-content (0 vs. 1 at.% Ru, resp.).

	Astra 1–20		Astra 1–21	
	at.%	wt.%	at.%	wt.%
Al	13.50	5.88	13.50	5.84
Co	9.00	8.56	9.00	8.50
Cr	6.00	5.03	6.00	5.00
Mo	0.60	0.93	0.60	0.92
Re	2.00	6.01	2.00	5.97
Ru	0.00	–	1.00	1.62
Ta	2.20	6.42	2.20	6.38
W	2.00	5.93	2.00	5.89
Ni (bal.)	64.70	61.24	63.70	59.88

Table 2
Heat-treatment process parameters.

Step	Heating rate [K/min]	Temperature [°C]	Holding time [h]	Cooling
Solutioning	4	1340	16	In air
1st annealing	4	1140	2	In air
2nd annealing	4	870	24	In air

2.2. Focused Ion Beam (FIB) – scanning electron microscopy (SEM) investigations

SEM-FIB investigations were conducted on a Helios NanoLab 600i instrument. The (0 0 1) planes of the γ/γ′ microstructure were observed with the use of a concentric backscattered (CBS) detector operating in an in-lens mode, accelerating voltage of 5 keV and a beam current of 0.69 nA. This method allowed for ultra-high resolution (UHR) imaging of TCP phases.

The three-dimensional (3D) inspection of the microstructure was possible by employing automated FIB sectioning and subsequent imaging with the use of backscattered detector (BSE) in UHR mode. A stack of 400 slices with the thickness of 20 nm each were collected by thinning the material with an ion beam current of 0.79 nA. The area of a single slice covered 100 μm^2, resulting in a total scanned volume of 800 μm^3 obtained in a reasonable time for ion thinning.

2.3. Image processing and analysis

The images obtained in SEM were binarized to reveal TCP phases only. The area fraction of TCP phases was calculated by counting the corresponding area of TCP phases and dividing it by the full imaged area. Each single value was obtained by analyzing 3–5 images.

The real 3D morphology of TCP phases was obtained with the use of FEI SAS AvizoFire software. The slices were added one by one to reconstruct the full scanned volume. Algorithms for alignment were applied to eliminate problems with drift and bring the slices to the same x, y coordinates (z varies with the slice number). The morphology of TCP phases was extracted from the γ/γ′/TCP microstructure by applying grayscale thresholding algorithms.

2.4. Transmission electron microscopy investigations

The Astra 1–20 TEM sample was prepared by grinding and polishing disks to a thickness of about 80 μm followed by a dimple grinding step to a thickness of only a few μm. To obtain high quality samples for HRTEM investigations the sample was thinned to electron transparency by using Ar^+ ions with a final polishing step at −20 °C and ion energy of 700 eV.

The sample of Astra 1–21 was prepared in a FEI Helios NanoLab 600i dual beam instrument by employing a standard TEM lamella lift out technique. For a final milling step, both sides of the lamella were polished using a voltage of 2 kV to obtain a sample with a thickness below 50 nm.

The diffraction patterns for the TCP-phase analysis were acquired on Ditabis imaging plates at a Philips CM30 operating at an accelerating voltage of 300 kV. For the acquisition of the HRTEM images an image-side aberration-corrected FEI Titan^3 80–300 operating at 200 kV was employed.

2.5. Atom probe tomography

APT specimens were prepared using a dual-beam focused-ion-beam (FIB) system (FEI Helios Nanolab 600) and the site-specific lift-out technique described in [24]. To reduce implantation of Ga ions to a negligible level, a low energy (5 keV) Ga beam was used for final shaping of the APT tips. APT analyses were done using a reflectron-equipped local electrode atom probe (LEAP™ 3000X HR, Cameca Instruments) in pulsed laser mode. Laser pulses of 532 nm wavelength, 12 ps pulse length, 0.4 nJ energy, and 100 kHz frequency were applied, while the base temperature of samples was kept at about 40 K. Data reconstruction and analysis were performed using the Cameca IVAS™ 3.6.6. software package. The first subset of ~1 mio. collected ions was discarded from the data analysis to exclude Ga ions implanted during FIB-milling.

3. Results

3.1. Microstructure evolution

3.1.1. Early stage – preference of dendrite core precipitation

Fig. 1 represents the overall view of the dendrite structure of the material Astra 1–20 decorated by TCP phases in the intermediate stage of their growth. The TCP phases are imaged as white particles, while the γ/γ′ microstructure corresponds to black color. Apparently one can distinguish brighter and darker regions in Fig. 1, i.e. regions of higher or lower white particle concentration. The brighter regions correspond to dendrite cores while the darker ones belong to interdendritic regions. This indicates an inhomogeneous density of TCP phases due to segregation. One should mention that for the purpose of clarification the pixels corresponding to TCP phases were slightly dilated digitally, but the findings above are not affected.

Our observation is well in accordance with the knowledge that TCP phases precipitate preferentially in the regions of higher Re concentration, i.e. dendrite cores [13]. Precipitation of TCP phases in interdendritic regions takes place at the later stages, as described in following subsections.

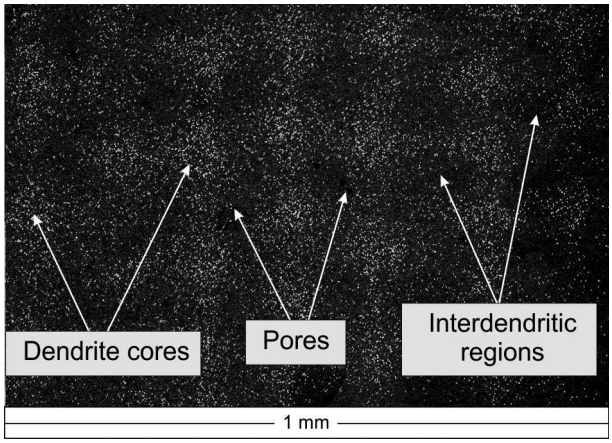

Fig. 1. TCP phase precipitation in the alloy Astra 1–20 (no Ru addition) after 1000 h of annealing at 950 °C. SEM micrograph with TCP phases appearing bright. The brighter regions indicating strong TCP precipitation correspond to dendrite cores. The micrograph was adjusted digitally to enhance the contrast observed from TCP phases.

3.1.2. Morphology and crystallography of the TCP phases

Two types of TCP phases have been observed in this paper, σ- and μ-phase. The details of their morphology and crystallography are listed in Table 3.

As can be seen in Fig. 2, in the early stages of precipitation SEM images of the (100) surface reveal TCP phases as "needles" inclined by 45° to γ/γ′ phase boundaries. These "needles" are in fact plate-like phases aligned parallel to {111} matrix planes (Fig. 2b). A more detailed study of the morphology of plate-like TCP phases is described elsewhere [15]. As revealed by TEM selected area diffraction patterns, the plate-like TCP phases represent the tetragonal σ-phase with the orientation relationship $(111)_\gamma//(001)_\sigma$ and $[110]_\gamma//[110]_\sigma$. Furthermore, the σ-phase exhibits three distinct crystal orientations or grains, rotated along the $<001>_\sigma$ or the $<111>_{\gamma/\gamma'}$ axis. As each distinct grain has the direction $[110]_\sigma$ parallel to one of the three equivalent [−110], [−101], [0–11] directions in the γ/γ′ microstructure, the σ-phase forms the characteristic twelve-spot diffraction pattern shown in Fig. 2c. Our findings are consistent with the results reported by Rae and Reed [11] and Darolia et al. [9] obtained in other Ni-based superalloys. The orientation relationship $(001)_\sigma//(111)_{\gamma/\gamma'}$ found in TEM is also in a very good agreement with the 3D inspection of the microstructure based on FIB tomography.

The other distinct type of TCP phase observed in this investigation is of more blocky morphology when studied in 2D. More careful 3D investigation reveals a lath like geometry with varying lath length. The lath-like TCP phases are characteristic for the later stages of precipitation. The lath-like TCP phases appear very often in close vicinity of plate-like σ-phase (Fig. 3a) suggesting that the growth of lath-like precipitates originates from the plate-like σ-phase. TEM investigations reveal that at the temperature of 950 °C the lath-like TCP phases are rhombohedral μ-phase with the orientation relationship $(111)_\gamma//(100)_\mu$ and $[110]_\gamma//[001]_\mu$. $[001]_\mu$ is the growth direction of μ-type lath-like particles.

The role of the plate-like σ-phase in the growth of lath-like μ-phase is well documented by 3D observations (see Fig. 4) and agrees well with the data obtained by TEM. On the basis of the orientation relationships σ/γ and μ/γ the following relationships can be deduced: $(111)_\gamma//(001)_\sigma//(100)_\mu$ and $[110]_\gamma//[110]_\sigma//[001]_\mu$.

3.1.3. Evolution of TCP phases with time

In Fig. 5a, c, e, g a time-dependent evolution of TCP phases in the dendrite core for the alloy Astra 1–20 (no Ru) is shown. After 500 h of annealing at 950 °C (Fig. 5a) TCP phases are already present. The interdendritic regions are still almost free of TCP phases, as can be seen in Fig. 1. At this stage of precipitation, TCP phases are of σ-type and exhibit plate-like morphology, as shown in Fig. 2b. With further annealing up to 1000 h (Fig. 5c), the density of plate-like particles increases. Additionally, the first μ-precipitates of lath-like morphology are observed, but their amount is much lower than that of the plate-like particles of σ-phase. The μ-phases appear in the close vicinity of the plate-like phases, as described in section 3.1.2. After 1500 h of

Table 3
Details of the morphology and crystallography of TCP phases observed in this work.

No.	Phase	2D appearance	3D appearance	Orientation relationship	Lattice type
1.	σ	Needle	Plate	$(111)_\gamma//(001)_\sigma$, $[110]_\gamma//[110]_\sigma$	Tetragonal
2.	μ	Blocky	Lath	$(111)_\gamma//(100)_\mu$, $[110]_\gamma//[001]_\mu$	Rhombohedral

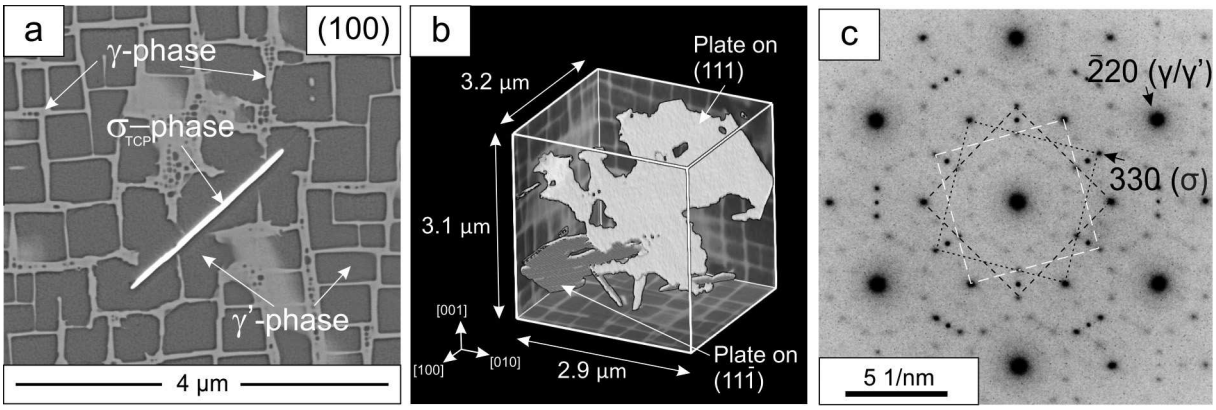

Fig. 2. Astra 1–20 (no Ru addition) after 1000 h of annealing at 950 °C with (a) TCP σ-phase of plate-like morphology imaged in SEM on (100) plane of γ/γ′ and (b) the 3D SEM-FIB-visualization of the σ-phase. The faces of the cube in (b) represent the family of (100) planes. When the plate-shaped σ-phase is sectioned by a (100) plane, it appears needle-like; (c) TEM diffraction pattern showing orientation relationship between TCP σ-phase and the γ/γ′ microstructure. The characteristic 12 spot diffraction pattern of the σ-phase is due to four fold symmetry of its tetragonal structure and polycrystalline structure. The three distinct orientations of σ-phase subgrains are marked with black or white dashed-line rectangles.

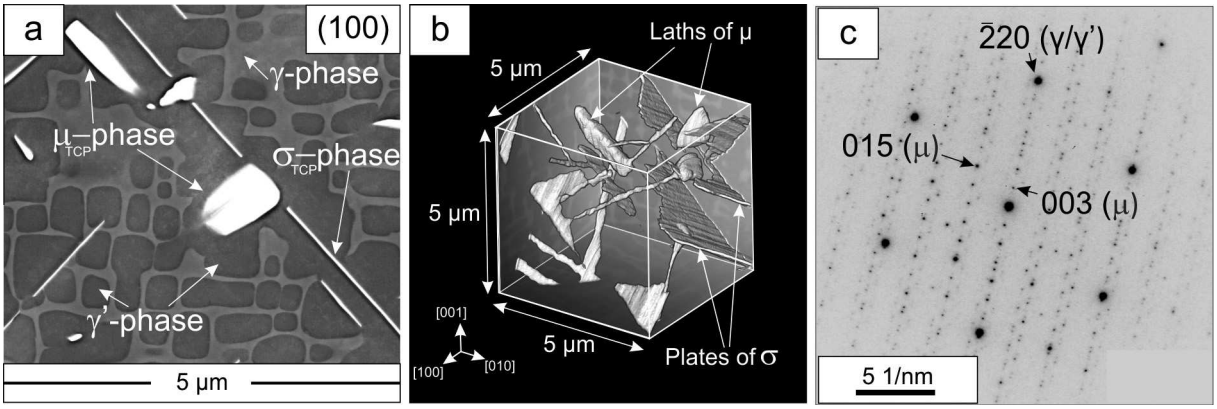

Fig. 3. Astra 1–20 (no Ru addition) annealed 1500 h at 950 °C with (a) TCP μ-phase of blocky morphology imaged in SEM on (100) plane of γ/γ′ close to the plates of σ-phase and (b) the 3D visualization of the blocky μ-phase, revealing in fact a lath-like particle. The faces of the cube represent the family of (100) planes; (c) TEM diffraction pattern showing orientation relationship between TCP μ-phase and γ/γ′ microstructure.

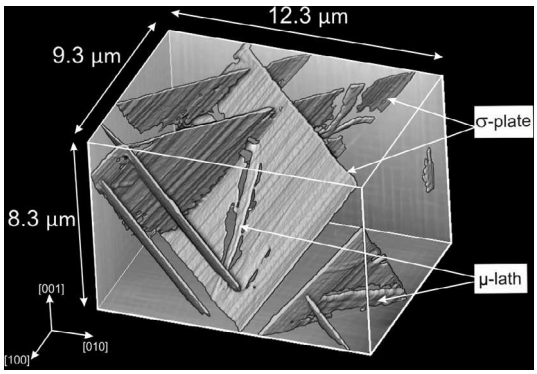

Fig. 4. 3D visualization of the lath-like μ-phase growing at the expense of plate-like σ-phase in the alloy Astra 1–21 (1 at.% Ru). The plates of σ-phase are much larger in size than in Fig. 2b, which is caused by the addition of Ru to the alloy.

annealing (Fig. 5e) a pronounced increase can be observed regarding the density and volume fraction of the μ-phase. It seems to grow at the expense of preexisting plate-like precipitates of σ type. Thus, fragmentation of σ-plates is observed when the laths of μ-phase grow. Moreover, one can observe dissolution of the γ-phase close to the TCP phases, i.e. they are surrounded by a thin γ′-phase envelope (local matrix). After 2000 h (Fig. 5g) the volume fraction of TCP phases increases further. The γ′-phase envelopes grow thicker and the γ/γ′ microstructure seems to be locally destabilized. Although precipitation of TCP phases advances with time in interdendritic regions too, the fraction of brittle TCP particles remains the highest in the dendrite cores.

The time-dependent growth of TCP phases for the alloy Astra 1–21 (1 at.% Ru) follows a very similar sequence as for the alloy without Ru. Nevertheless, a number of distinctions can be identified. The first difference lies in the incubation time for precipitation. When 1 at.% of Ru is present, only few σ-phase particles are observed after 500 h of annealing. Pronounced precipitation in the dendrite cores takes place after 1000 h of annealing (Fig. 5d).

The second significant difference lies in the area fraction of TCP phases. As shown in Fig. 5 at any time of annealing the alloy with higher Ru-content exhibits a significantly lower content of TCP phases.

The third difference becomes apparent by comparing the dimensions of precipitates in the alloys Astra 1–20 and 1–21. The addition of 1 at.% of Ru results in the growth of precipitates which are considerably bigger than in the Ru-free alloy (Fig. 5a, d). On the other hand, the density of σ-phase particles is reduced with addition of Ru, i.e. Ru promotes growth of fewer but bigger precipitates.

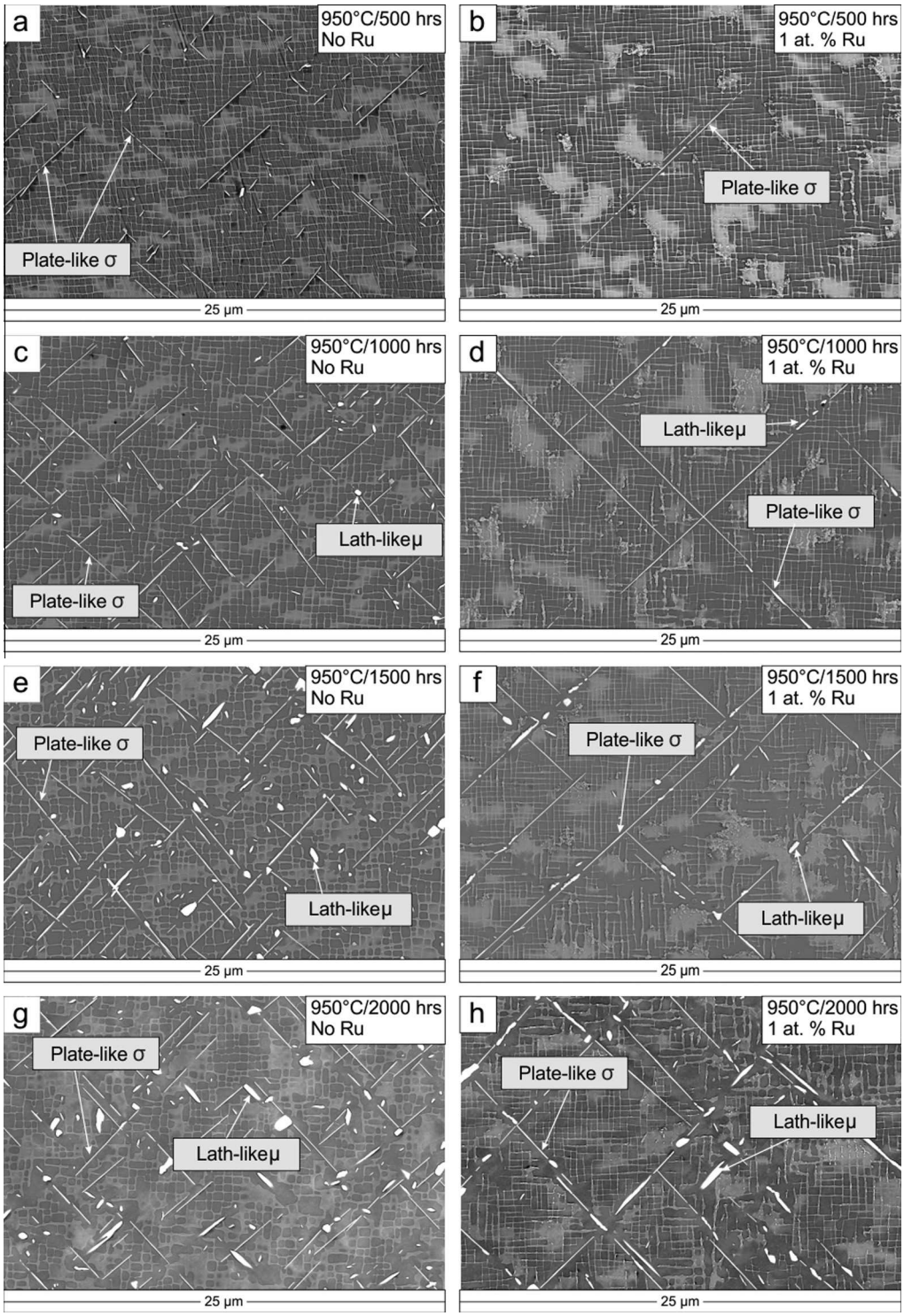

Fig. 5. The microstructure of Ni-based superalloys Astra 1–20 (on the left, no Ru) and Astra 1–21 (on the right, 1at.% Ru) in the dendrite core sectioned along (1 0 0) planes of γ/γ′ phases after isothermal annealing at 950 °C for (a, b) 500 h; (c, d) 1000 h; (e, f) 1500 h and (g, h) 2000 h. The content of Ru varies from (a, c, e, g) 0 to (b, d, f, h) 1 at.%. TCP phases are imaged as white particles of needle- or block-like morphology, being in fact plate- and lath-like particles, resp. Ru-addition results in fewer, but larger precipitates.

3.2. Quantitative analysis of precipitation

3.2.1. Area fraction of TCP phases

In Fig. 6 the area fraction of TCP phases is plotted versus time. The data obtained experimentally from Astra 1–20 (no Ru) and Astra 1–21 (same alloy, but 1 at.% Ru) are given as rectangular or circular points, respectively. The plotted lines represent the data fitting by use of the Johnson–Mehl–Avrami equation. For comparison, the data published earlier in [16] obtained at 1050 °C are also plotted on the graph. Additionally, the equilibrium content of TCP phases calculated with ThermoCalc (version 3.1, ThermoCalc, Stockholm) using the commercially available databases TTNi8

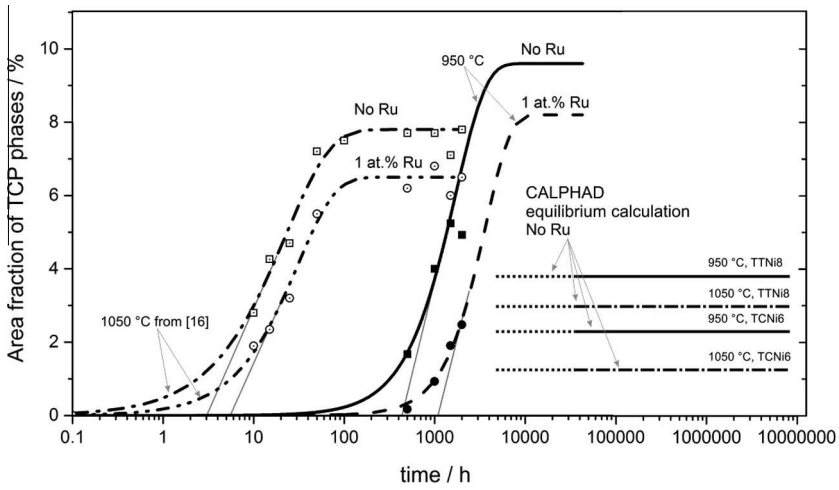

Fig. 6. Area fraction of TCP phases as a function of time for the alloys Astra 1–20 and Astra 1–21 with 0 and 1 at.% of Ru, resp. Data were obtained experimentally from SEM micrographs taken in dendrite cores. The curves correspond to Johnson–Mehl-Avrami fitting. The straight lines (tangents) determine graphically the initial rapid growth rate and incubation time. Data obtained at 1050 °C are taken from [16]. Ru leads to a smaller equilibrium volume fraction and more sluggish precipitation behavior. The straight horizontal lines in the figure correspond to the equilibrium content of TCP phases calculated with ThermoCalc (only for the no-Ru alloy, with the addition of Ru the result is about the same). They do not match the experimental data.

[25] and TCNi6 [26] is indicated by straight horizontal lines (only the alloy Astra 1–20; the data are overlapping with addition of Ru, i.e. the values are the same).

At the temperature of 1050 °C, incubation stage, rapid growth stage and equilibrium can be clearly distinguished. The rapid growth rates are graphically shown by the tangents to the curves drawn in Fig. 6. Their intersections with the time axis determine the incubation time. Equilibrium area fractions are indicated by the plateau of the non-linear curves. Complete precipitation of TCP phases is observed within 2000 h.

One can compare the equilibrium content of TCP phases obtained experimentally with those calculated with ThermoCalc. As measured, the equilibrium area fraction is reduced from 7.8% to 6.5% by the addition of Ru. According to calculations the equilibrium area fraction of TCP phases depends on the database and equals 3.0% or 1.2% for the database TTNi8 or TCNi6, respectively, regardless of Ru content. As can be seen, neither database TCNi6 nor TTNi8 gives results in accordance with experimental data. The temperature function obtained using the database TTNi8 is employed to fit the data obtained experimentally at 950 °C by Jo hnson–Mehl–Avrami curves. This allows for the calculation of TCP equilibrium fraction at 950 °C.

On the basis of the data obtained at 950 °C as well as 1050 °C the Ru influence on the TCP phase precipitation becomes evident. The rapid growth rate does not seem to be significantly affected by the addition of 1 at.% of Ru. However, at any time of isothermal annealing the content of TCP phases is reduced when Ru is present in the alloy.

Evidently, Ru has also a strong influence on the incubation time of TCP phase growth, i.e. the nucleation of σ-phase. At 950 °C for the Ru-free alloy, the incubation time is in the range of 450 h, while with the addition of 1 at.% of Ru this range is shifted to 1000 h. At 1050 °C, the incubation time is prolonged from 3 to 6 h by the addition of Ru.

3.2.2. Particle density and dimensions of sigma phase

In Fig. 7a the number of TCP particles (σ- and μ-phase together) per unit area is plotted as a function of time. As can be seen for the alloy Astra 1–20 (no Ru), the TCP particle density increases with time till 1500 h followed by a slight decrease. The steepest slope, i.e. the most rapid nucleation rate is found in the beginning, as the nucleation rate can only decrease with time as the driving force diminishes. The increase between 500 and 1500 h is influenced mostly by two factors. Besides nucleation of new particles of the σ-phase, the first particles of the μ-phase are formed. As μ-phase particles originate at the σ-phase plates, they lead to fragmentation of existing σ-plates, thus increasing significantly particle density. The drop between 1500 and 2000 h occurs most likely due to the growth of μ-phase at the expense of σ, i.e. σ-phase is gradually dissolved. General Ostwald ripening might also contribute.

The study of the average size of TCP-phase dimensions in Fig. 7b confirms our interpretation. One should note that only the dimensions of σ-phase plates are taken into account. The average length of σ-particles increases till 1000 h and then decreases.

The trend obtained in the alloy Astra 1–21 (with addition of Ru) is similar. However, the TCP particle density remains close to zero until 500 h and then increases significantly until 2000 h (Fig. 7a). Nevertheless it is always below the values obtained for the Ru-free alloy.

Although the number of particles per unit area is reduced by a factor of ~6, the size of σ-plates is considerably larger when Ru is present. This finding strongly suggests that Ru controls the incubation and nucleation stage of σ-phase. Moreover, the drop after 1500 h is much more pronounced in the alloy Astra 1–21. This is most likely an effect of the σ-plates fragmentation when μ-phase starts to grow.

3.3. Interface characteristic

As evidenced in paragraph 3.1.3, precipitation of TCP phases drives the dissolution of the γ-matrix phase. Hence, TCP phases are surrounded locally by the γ′-phase, which takes over the role of matrix. TEM and HR TEM investigations confirmed that the first phase to precipitate in the alloys Astra 1–20 (no Ru) and Astra 1–21 (1 at.% Ru) is the tetragonal σ-phase (Fig. 2c). Fig. 8 shows TEM and HR TEM images of σ-phase precipitates taken along $a < 110 >_{\gamma/\gamma'}$ zone axis. This allows imaging the σ/γ′ interface edge on and, therefore, investigating its characteristics.

As can be seen in Fig. 8c, the interface between σ- and γ′-phase is fully coherent and only isolated steps can be found occasionally (not shown in the image). It is interesting to note that the σ-precipitates are not perfect single crystals but exhibit distinct

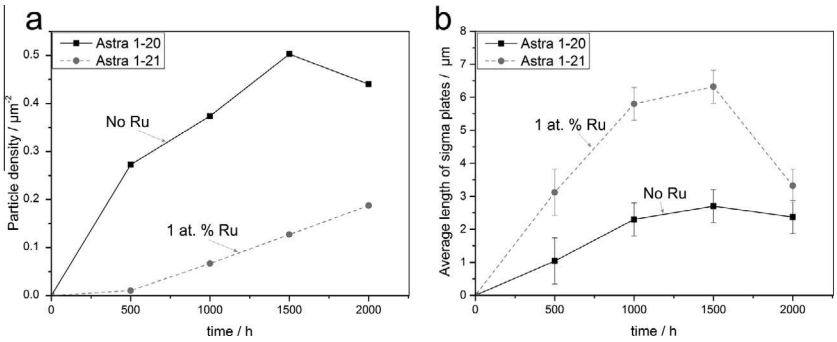

Fig. 7. (a) The particle area density of TCP phases as a function of time for the alloys Astra 1–20 and Astra 1–21 with 0 and 1 at.% of Ru, resp. Up to 1000 h the particle population consists exclusively of the σ-phase, while in the later stages, σ- and μ-phases appear and are counted together; (b) The average length of σ-phase plates for the alloys Astra 1–20 and 1–21. When Ru is present, the size of σ-precipitates is larger and the number per unit area is smaller. The drop after 1500 h corresponds to fragmentation of σ-plates caused by μ-phase precipitation.

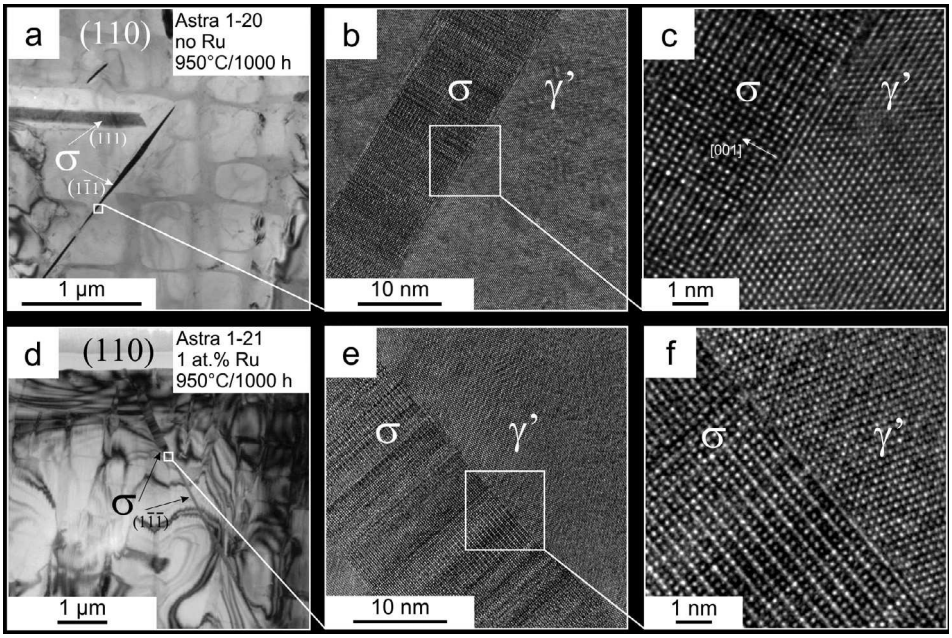

Fig. 8. TEM and HRTEM images of the σ/γ′ interface obtained in a <1 1 0> γ/γ′ zone axis in the alloys containing (a–c) no Ru (Astra 1–20) and (d–f) 1 at.% Ru (Astra 1–21). The σ/γ′ interface is fully-coherent independent of the Ru-content.

columnar grains rotated around the $<100>_{\sigma}$ axis (see Fig. 2c) running perpendicular to the σ/γ′ interface. The grain boundaries also running perpendicular to the σ/γ′ interface can be recognized in Fig. 8b and e by the varying contrast in HRTEM images. In spite of the existence of three different orientation variants, the coherency is always perfectly developed.

With the addition of Ru no significant differences in the coherency can be observed, i.e. the interface σ/γ′ reveals the same fully-coherent characteristic in the alloy Astra 1–21 (Fig. 8f). Therefore, at this point it can be ruled out that Ru influences the interface in such a way that interfacial energy is increased.

There are no dislocation networks observed close to the σ/γ′ interface, indicating good lattice fit between σ- and γ′-phases in both alloys. In this context an observation by Rae and Reed [11] is interesting who pointed out that the polycrystalline nature of the σ-phase might serve to accommodate misfit strains. The discussion above refers to the σ/γ′ interface. As far as the σ/γ interface is concerned, some Ru influence on lattice misfit is likely [27] due to the increased γ-lattice parameter with the addition of Ru [28].

3.4. Chemical composition analysis

3.4.1. Partitioning of ruthenium

Fig. 9 presents information about the partitioning of elements in the alloy Astra 1–21 (1 at.% Ru) after 1000 h of annealing at 950 °C. It can be noted that Al, Ta and Ni, as γ′-formers partition preferentially to γ′-phase. Elements like Mo, Cr, W and especially Re, as solid solution strengtheners, segregate to the γ-phase. Ru partitions to the matrix-phase as well. It does not share, however, the strong tendency of Re to enter the σ-phase.

Our recent investigations [27] show that Ru has no preference for the σ/γ′ phase boundary and does not promote either lower or stronger partitioning of any other elements to the interface σ/γ′.

Fig. 10 presents the chemical composition of TCP σ- and μ-phases in the alloys Astra 1–20 (no Ru) and Astra 1–21 (1 at.% Ru) after 2000 h of annealing at 950 °C. The composition of σ-phase does not vary with time within the error of the analysis. As can be seen from the graph, Ru does not affect strongly the chemical composition of either σ- or μ-phase. There are minor changes found regarding the content of Ni, Cr or Mo, but the

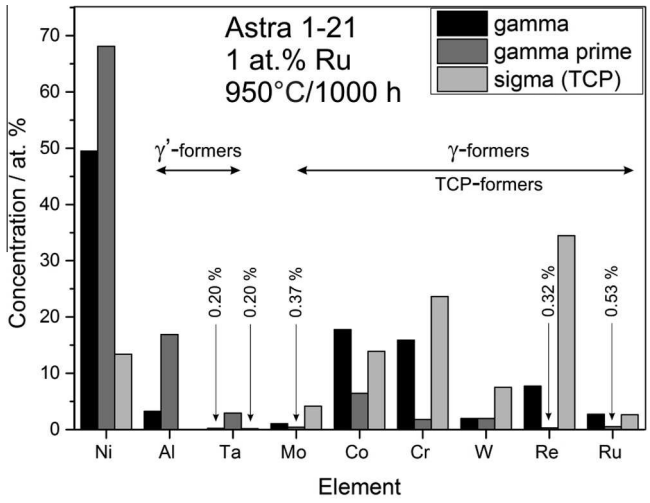

Fig. 9. Chemical composition of σ-, γ- and γ′- phases obtained via APT investigation in the alloy Astra 1–21 after 1000 h of annealing at 950 °C. Ru goes preferably and in equal amounts to γ- and σ-phases. All the other elements segregate in the usual way as γ′- and γ-phase forming elements.

difference is not essential according to the stability of TCP phases. The highest difference is found in case of Ru and Re contents. Re content in the σ-phase is decreased by around 2.5 at.% in comparison with the Ru-free alloy. This value corresponds very well to Ru increase in σ-phase. The effect can be caused by Re–Ru site occupancy competition. A similar effect is observed in the case of μ-phase.

Moreover, the compositions of individual σ- and μ- phases do not differ a lot. Ru partitions in a similar way to both TCP phases. Compared to the σ-phase, the μ-phase exhibits reduced Cr and Re content while W, Co, Ni and Mo are increased. However, the compositions are similar. This is interesting since it was previously reported that μ-phase composition is low in Re [11] and high in W and Co, which is not the case in the present study. This discrepancy can be explained by the fact that investigated μ-phases were growing at the expense of σ-plates.

3.4.2. Composition of γ- and γ′-phases

The chemical composition of γ- and γ′-phases was measured within the dendrite cores. In the case of the alloys with the precipitated σ-phase, i.e. after 1000 or 2000 h of annealing, the data points were taken relatively far away from neighboring TCP phases. However, the general location within the dendrite core was maintained to make the data comparable.

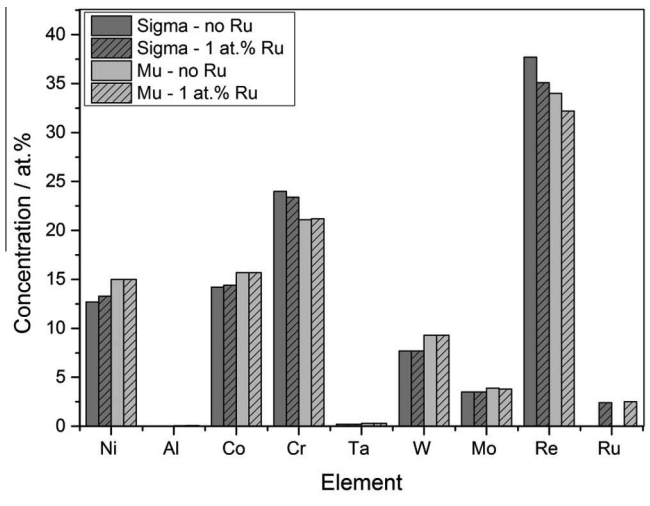

Fig. 10. Chemical composition of TCP σ- and μ- phases obtained via APT investigation in the alloys Astra 1–20 and Astra 1–21, containing 0 and 1 at.% Ru respectively. No major effect from Ru is observed.

In Fig. 11a the chemical compositions of the γ′-phase are given. Ru addition does not change the chemical composition of the γ′-phase significantly. Only minor changes in concentrations of Ni and Al with the addition of Ru are observed. In particular, there is no enrichment of Re within the γ′-phase when Ru is present in the alloy. This is valid for both heat treatments, as age hardened and after annealing at 950 °C, as the γ′-phase composition varies with time within the error of the analysis. Our data indicate that reverse partitioning effect as reported in the literature does not occur in this class of alloys.

Fig. 11b represents, in turn, the chemical compositions of the γ-phase for the same heat treatment stages as above. In the case of γ-phase composition, we observe some changes with the addition of Ru. First of all, the concentration of Ni is reduced. This is the result of substituting Ru at the expense of Ni in the nominal composition of the alloy. The second difference is an increased Re concentration. When Ru is present in the alloy, γ-phase is enriched in Re by about 1 at.%. Although the concentration of Re drops slightly as a function of time, which is most likely caused by precipitation of TCP phases, its enrichment in the γ-phase of the Ru-containing alloy remains.

4. Discussion

4.1. Effect of Ru on driving force and interface

Ru has been observed in our work to slow down the speed of TCP phase transformation and to reduce the equilibrium volume fraction of TCP phases. More precisely, addition of Ru extends the incubation time for the growth of σ- phase (Fig. 6) from around 450 h for the no-Ru alloy to 1000 h for the alloy containing 1 at.% of Ru. Further, with the addition of Ru the number of TCP precipitates per volume is reduced by a factor of ∼6, while their size is increased by a factor of ∼2.5. These factors result in reduced volume fraction of TCP phases. As measured at 1050 °C, addition of 1 at.% Ru reduces the equilibrium volume fraction of TCP phases from 7.8% to 6.5%.

Quite in general, precipitation is affected by diffusivity, driving force and interface effects. Precipitation of TCP phases is controlled by Re diffusion as the Re diffusion coefficient is very low. Hobbs et al. [5] reported that the diffusion rate of Re is not influenced by Ru. This is why we will discuss only driving force and interface effects in the following.

The reduced equilibrium volume fractions (Fig. 6) point directly to a reduced driving force for TCP precipitation if Ru is added. This finding is contrary to thermodynamic calculations, Fig. 6 and Ref. [16]. According to them Ru has no influence on the driving force for TCP phase precipitation. Obviously, none of the available thermodynamic databases is able to predict equilibrium of TCP phases correctly, particularly as a function of Ru. The increased concentration of Re in the γ-matrix phase (Fig. 11b) indicates as well a reduced driving force for TCP phase precipitation.

There are no major differences in orientation relationship found for the addition of Ru. Moreover, Ru does not alter the composition of either the bulk (Fig. 10) or the interface of the σ-phase [27]. Based on these findings there is no effect of change of binding energy on interfacial energy to be expected because of Ru addition.

In previous work, Heckl et al. reported an increase in γ- and γ′-lattice parameters when 2 at.% of Ru is present in the alloy [28]. A similar effect, but less pronounced, is expected in the alloy Astra 1–21. As far as the σ-phase lattice parameter is concerned Ru

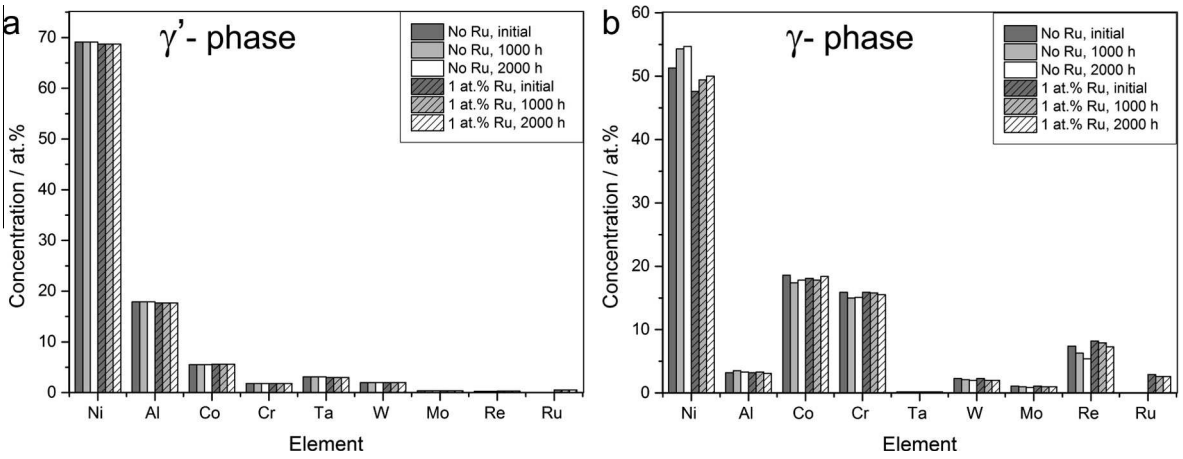

Fig. 11. Chemical composition of (a) γ′-phase and (b) γ-phase obtained via APT investigation in the alloys Astra 1–20 and Astra 1–21, containing 0 and 1 at.% Ru respectively. For comparison there are values given for the samples after standard heat-treatment (initial) and after annealing for 1000 h and 2000 h at 950 °C. There are no significant changes in the chemical composition of the γ′-phase observed with the addition of Ru and with exposure to temperature. In the case of γ-phase an increase in Re content is detected with the addition of Ru. This characteristic is visible in both initial stage and after annealing until 2000 h at 950 °C.

is assumed to partition to σ-phase at the expense of Re, but this should not affect σ-phase lattice parameters due to similarities in the atomic radii of both elements [27]. The increased γ-phase lattice parameter is expected to result in a larger γ/σ lattice misfit ($\gamma_{<431>}/\sigma_{<100>}$) as determined in [11]. In other words, Ru might lead to higher coherency strains making the formation of nuclei more difficult.

4.2. Effect of Ru on nucleation and growth rate of σ-phase

Reduction of the driving force translates into a lower nucleation rate and a lower growth rate of precipitates. Results in Fig. 7b imply that growth of σ-plate length is not decelerated but accelerated by Ru addition. In consequence the retarding effect of Ru on TCP phase precipitation (transformed volume fraction) must be mainly due to a reduction in nucleation rate rather than growth rate. Also the decreased number of precipitates per unit area (Fig. 7a) indicates a lower nucleation rate if Ru is added.

In addition to the effect of reduced driving force due to Ru there could be an effect of increased coherency strains to bring down the nucleation rate, as discussed in the previous paragraph.

5. Conclusions

The aim of the present study was to find the mechanism of Ru influence on the precipitation of TCP phases in the experimental alloy Astra1–20 containing 2 at.% Re. Based on the investigations the following conclusions are stated:

1. TCP phases precipitate in a sequence with the plate-like tetragonal σ-phase precipitating first in this class of alloys;
2. The observed orientation relationship between γ-, σ- and μ-phases promotes nucleation of TCP phases and their growth;
3. Ru influences precipitation of TCP phases, resulting in retardation of phase transformation and smaller equilibrium volume fraction. The number of particles per unit area is significantly decreased (min. by a factor of 6) due to Ru addition. The length of σ-phase plates is increased by the addition of Ru (max. by a factor of 2.5). In terms of transformed volume fraction, the faster growth of σ-particles by addition of Ru is overcompensated by the smaller number of particles nucleated.
4. A reverse partitioning effect is not detected within the range of investigated materials;
5. The driving force for precipitation is decreased by Ru addition as indicated by the smaller equilibrium volume fraction and the higher Re matrix concentration.
6. Although Ru does not influence significantly the σ/γ′ interface energy it probably increases the misfit strain energy by increasing the σ/γ lattice misfit;
7. As a result of 5 and 6 the nucleation rate of TCP precipitates is decreased because of Ru.

Acknowledgments

The financial support of the German Science Foundation (DFG) within the Collaborative Research Center SFB/Transregio 103 “From Atoms to Turbine Blades – a Scientific Approach for Developing the Next Generation of Single Crystal Superalloys”, projects A4, A7, B1 and WSP, as well as within the Research Training Group 1229 “Stable and Metastable Multiphase Systems at High Temperature” is gratefully acknowledged.

References

[1] A.F. Giamei, D.L. Anton, Rhenium addition to a Ni-base superalloy: effects on microstructure, Metall. Trans. A 16A (1985) 1997–2005.
[2] G.L. Erickson, The development and application of CMSX®-10, in: R.D. Kissinger, D.J. Deye, D.L. Anton, A.D. Cetel, M.V. Nathal, T.M. Pollock, D.A. Woodford (Eds.), Superalloys 1996, Metals and Materials Society, Warrendale, The Minerals, 1996, pp. 35–44.
[3] D. Blavette, P. Caron, T. Khan, An atom-probe study of some fine-scale microstructural features in Ni-based single crystal superalloys, in: S. Reichman, D.N. Duhl, G. Maurer, S. Antolovich, C. Lund (Eds.), Superalloys 1988, The Metallurgical Society, Warrendale, 1988, pp. 305–314.
[4] M.S.A. Karunaratne, P. Carter, R.C. Reed, Interdiffusion in the face-centred cubic phase of the Ni–Re, Ni–Ta and Ni–W systems between 900 and 1300 °C, Mater. Sci. Eng. A A281 (2000) 229–233.
[5] R.A. Hobbs, M.S.A. Karunaratne, S. Tin, R.C. Reed, C.M.F. Rae, Uphill diffusion in ternary Ni–Re–Ru alloys at 1000 and 1100 °C, Mater. Sci. Eng. A A460–461 (2007) 587–594.
[6] A. Heckl, S. Neumeier, M. Göken, R.F. Singer, The effect of Re and Ru on γ/γ′ microstructure, γ-solid solution strengthening and creep strength in nickel-base superalloys, Mater. Sci. Eng. A A528 (2011) 3435–3444.
[7] A. Heckl, R. Rettig, R.F. Singer, Solidification characteristics and segregation behavior of Nickel-Base superalloys in dependence on different Rhenium and Ruthenium contents, Metall. Mater. Trans. A 41A (2010) 202–211.
[8] R.A. Hobbs, S. Tin, C.M.F. Rae, R.W. Broomfield, C.J. Humphreys, Solidification characteristics of advanced Nickel-base single crystal superalloys, in: K.A. Green, T.M. Pollock, H. Harada, T.E. Howson, R.C. Reed, J.J. Schirra, S. Walston (Eds.), Superalloys 2004, Metals and Materials Society, Seven Springs, The Minerals, 2004, pp. 819–825.

[9] R. Darolia, D.F. Lahrman, R.D. Field, Formation of topologically closed packed phases in nickel base single crystal superalloys, in: S. Reichman, D.N. Duhl, G. Maurer, S. Antolovich, C. Lund (Eds.), Superalloys 1988, The Metallurgical Society, Warrendale, 1988, pp. 255–264.
[10] R.A. Hobbs, L. Zhang, C.M.F. Rae, S. Tin, Mechanisms of topologically close-packed phase suppression in an experimental ruthenium-bearing single-crystal nickel-base superalloy at 1100 °C, Metall. Mater. Trans. A 39A (2008) 1014–1025.
[11] C.M.F. Rae, R.C. Reed, The precipitation of topologically close-packed phases in rhenium-containing superalloys, Acta Mater. 49 (2001) 4113–4125.
[12] A.C. Yeh, S. Tin, Effects of Ru on the high-temperature phase stability of Ni-base single-crystal superalloys, Metall. Mater. Trans. A 37A (2006) 2621–2631.
[13] M.S.A. Karunaratne, C.M.F. Rae, R.C. Reed, On the microstructural instability of an experimental Nickel-based single-crystal superalloy, Metall. Mater. Trans. A 32A (2001) 2409–2421.
[14] M. Simonetti, P. Caron, Role and behavior of μ phase during deformation of a nickel-based single crystal superalloy, Mater. Sci. Eng. A A254 (1998) 1–12.
[15] K. Matuszewski, R. Rettig, M. Rasiński, K.J. Kurzydłowski, R.F. Singer, The three-dimensional morphology of topologically close packed phases in a high rhenium containing nickel based superalloy, Adv. Eng. Mater. 16 (2014) 171–175.
[16] K. Matuszewski, R. Rettig, R.F. Singer, The effect of Ru on precipitation of topologically close packed phases in Re-containing Ni base superalloys: Quantitative FIB-SEM investigation and 3D image modeling, in: J. Guedou, J. Chonne (Eds.), Proceedings of 2nd European Symposium on Superalloys and their Applications (Eurosuperalloys 2014), MATEC Web of conferences, 14 (2014), 129–134.
[17] A. Sato, H. Harada, T. Yokokawa, T. Murakumo, Y. Koizumi, T. Kobayashi, The effects of ruthenium on the phase stability of fourth generation Ni-base single crystal superalloys, Scripta Mater. 54 (2006) 1679–1684.
[18] K.S. O'Hara, W.S. Walston, E.W. Ross, R. Darolia, United States Patent 5482789, January 9, 1996.
[19] S. Neumeier, F. Pyczak, M. Göken, The influence of ruthenium and rhenium on the local properties of the gamma- and gamma prime-phase in nickel-base superalloys and their consequences for alloy behavior, in: R.C. Reed, K.A. Green, P. Caron, T.P. Gabb, M.G. Fahrmann, E.S. Huron, S.A. Woodard (Eds.), Superalloys 2008, Metals and Materials Society, Seven Springs, The Minerals, 2008, pp. 109–119.
[20] F. Pyczak, S. Neumeier, M. Göken, Temperature dependence of element partitioning in rhenium and ruthenium bearing nickel-base superalloys, Mater. Sci. Eng. A A527 (2010) 7939–7943.
[21] R. Rettig, R.F. Singer, Influence of ruthenium on topologically close packed phase precipitation in single-crystal Ni-based superalloys: numerical experiments and validation, in: E.S. Huron, R.C. Reed, M.C. Hardy, M.J. Mills, R.E. Montero, P.D. Portella, J. Telesman (Eds.), Superalloys 2012, Metals and Materials Society, Seven Springs, The Minerals, 2012, pp. 205–214.
[22] R. Rettig, A. Heckl, R.F. Singer, Modeling of precipitation kinetics of TCP-phases in single crystal nickel-base superalloys, Adv. Mater. Res. 278 (2011) 180–185.
[23] D.A. Porter, K.E. Easterling, M.Y. Sherif, Phase Transformations in Metals and Alloys, third ed., CRC Press, Boca Raton, 2009.
[24] K. Thompson, D. Lawrence, D.J. Larson, J.D. Olson, T.F. Kelly, B. Gorman, In situ site-specific specimen preparation for atom probe tomography, Ultramicroscopy 107 (2007) 131–139.
[25] N. Saunders, M. Fahrmann, C. Small, The application of CALPHAD calculations to Ni-based superalloys, in: T.M. Pollock, R.D. Kissinger, R.R. Bowman, K.A. Green, M. McLean, S. Olson, J.J. Schirra (Eds.), Superalloys 2000, Metals and Materials Society, Seven Springs, The Minerals, 2000, pp. 803–811.
[26] N. Dupin, B. Sundman, A thermodynamic database for Ni-base superalloys, Scand. J. Metall. 30 (2001) 184–192.
[27] Z. Peng, I. Povstugar, K. Matuszewski, R. Rettig, R.F. Singer, A. Kostka, P. Choi, D. Raabe, Effects of Ru on elemental partitioning and precipitation of topologically close-packed phases in Ni-based superalloys, Scripta Mater. 101 (2015) 44–47.
[28] A. Heckl, S. Neumeier, S. Cenanovic, M. Göken, R.F. Singer, Reasons for the enhanced phase stability of Ru-containing nickel-based superalloys, Acta Mater. 59 (2011) 6563–6573.